DETECTOR MAGNETS FOR CHARGED PARTICLE MOMENTUM MEASUREMENT

G. Arduini and G. Petrucci

Abstract

Basic formulae related to the momentum measurement of charged particles by tracking devices in magnetic fields and typical detector magnet geometries are briefly revised. From these, guidelines are worked out for the determination of the basic specifications (yoke size, excitation current, conductor type and size, cooling) both for normal and superconducting magnets. The problem of magnetic shielding of components placed near big detector magnets is also considered.

Submitted to ICFA Instrumentation Panel as contribution to Detector Data Digest

1   Charged particle momentum measurement

The measurement of the momentum of charged particles is generally accomplished by means of tracking devices allowing the determination of the deflection angle, radius of curvature or sagitta of the trajectories of the particles in a magnetic field.

The relevant formulae in the measurement of the particle momentum p by means of magnetic fields are given below [YUA61]:

$$p \simeq 0.3qBR\sin\alpha$$

$$p \simeq \frac{0.3qBR_\perp}{\sin\alpha}$$

$$p \simeq 0.3qB\left(\frac{C^2\sin\alpha}{8S} + \frac{S}{2\sin\alpha}\right) \quad \text{(uniform field along the trajectory)}$$

$$p \simeq 0.3q\frac{\int B_\perp dl}{\theta}$$

p in GeV/c; B in T; R, $R_\perp$, C and S in m; θ in rad and $\int B_\perp dl$ in $T \cdot m$, where:

- B is magnitude of the magnetic induction **B**;
- R is the radius of curvature of the trajectory in space;
- α is the angle between the tangent to the trajectory in any point and the direction of the magnetic induction **B**;
- q is the charge of the particle in units of electron charge magnitude;
- $R_\perp$ is the radius of curvature of the trajectory projected in the plane perpendicular to **B**;
- C is the length of the chord connecting two points in the trajectory and S is the related sagitta;
- θ is the bending angle provided by the transverse integrated field $\int B_\perp dl$.

The momentum resolution achievable by means of spectrometer magnets is mainly determined by the spatial resolution of the tracking devices and by the multiple scattering in the media along the track of the particle, therefore:

$$\left(\frac{\Delta p}{p}\right)^2 = \left(\frac{\Delta p}{p}\right)^2_{res} + \left(\frac{\Delta p}{p}\right)^2_{ms}.$$

Three main methods for the determination of the particle momentum can be distinguished:

- *Measurement of the deflection angle* provided by a magnetic field perpendicular (main component $B_\perp$) to the average direction of the particles (e.g. in fixed target experiments with air-core dipoles or toroids and in the momentum analysis of high-energy muons by means of

iron-core toroids and dipoles).

The trajectories of the particles upstream and downstream the magnet can be determined each by means of a pair of planar position-sensitive detectors orthogonal to the average direction of the particles. The spatial resolution Δx of these detectors in the direction perpendicular to the magnetic field provides a contribution to the momentum error given by [KLE86]:

$$\left(\frac{\Delta p}{p}\right)_{res} \simeq 6.7 \frac{p}{q \int B_\perp dl} \frac{\Delta x}{h} \quad p \text{ in } GeV/c \text{ and } \int B_\perp dl \text{ in } T \cdot m$$

where h is the distance between the two detectors of each arm of the spectrometer. This is generally the main contribution to momentum errors in case of negligible multiple scattering.

The effect of multiple scattering may become relevant if any material is interposed along the trajectory of the particles, as, for example, in iron-core magnets or when the coils or the support structure partially or totally enclose the detection region (e.g. toroidal magnets with a uniformely distributed coil - see section 3.3). In this case [KLE86]:

$$\left(\frac{\Delta p}{p}\right)_{ms} \simeq \frac{0.05}{\beta \int B_\perp dl} \sqrt{\frac{L}{X_0}} \quad \int B_\perp dl \text{ in } T \cdot m$$

where L is the length of the track in the material and β is the relativistic parameter[1].

- *Measurement of the radius of curvature and of the angle α in a uniform magnetic field and in a uniform medium* by means of a least-squares fit to the coordinates of N equidistant points of the detected track (e.g. central tracking for storage ring experiments with solenoidal magnets). If $N > 10$ measurements are made along the trajectory [GLU63] [KLE86]:

$$\left(\frac{\Delta p}{p}\right)_{res} \simeq \frac{\Delta x \, p}{0.3qBL^2 \sin\alpha} \sqrt{\frac{K}{N+4}} \tag{1}$$

Δx and L in m; p in GeV/c and B in T, where:

- Δx is the tracking resolution in the plane perpendicular to the magnetic field;

- $K \simeq 320$ if a vertex constraint is applied at the origin of the track, otherwise $K \simeq 720$ [PDG94];

- L is the length of the track;

---

[1] If the particle traverses different materials $\sqrt{\frac{L}{X_o}}$ must be replaced with $\sqrt{\sum_i \frac{L_i}{X_{oi}}}$, where L_i is the length of the track in the i-th traversed material having radiation length X_{oi}.

and [PDG94]

$$\left(\frac{\Delta p}{p}\right)_{ms} \simeq \frac{0.06}{\beta B \sqrt{L X_o} \sin \alpha} \quad B \text{ in } T; \; X_o \text{ and } L \text{ in } m. \tag{2}$$

The loss in momentum resolution arising from the error $\Delta \alpha$ in the determination of the angle α has been neglected in expressions 1 and 2. The error $\Delta \alpha$ is due to the spatial resolution of the tracking device and to multiple scattering and provides the following contributions to momentum resolution, respectively [GLU63] [KLE86]:

$$\left(\frac{\Delta p}{p}\right)_{res} \simeq \frac{\Delta z}{L \tan \alpha} \sqrt{\frac{12(N-1)}{N(N+1)}} \tag{3}$$

$$\left(\frac{\Delta p}{p}\right)_{ms} \simeq \frac{0.009q}{p\beta \tan \alpha} \sqrt{\frac{L}{X_o}} \quad p \text{ in } GeV/c \tag{4}$$

where Δz is the spatial resolution of the tracking device in the direction parallel to the magnetic field. These terms should be added in quadrature to those in expressions 1 and 2, respectively.

- *Measurement of the sagitta* of the track of the particle in a uniform magnetic field by determining the coordinates of three equidistant points or three equidistant clusters of points. The latter technique is the most frequently used for high-energy muon spectrometry by means of air-core magnets. The track is measured at the entry of the magnetic field region (N_1 independent measurements) in its middle (N_2 independent measurements) and at its exit (N_3 independent measurements) with a resolution given by expression 1 with $N = N_1 + N_2 + N_3$ for a uniform magnetic field and a uniform medium [FAB94]. The contribution to momentum resolution due to multiple scattering is given by expression 2.

If the sagitta is determined by measuring the coordinates of only three points of the particle trajectory [KLE86]

$$\left(\frac{\Delta p}{p}\right)_{res} \simeq 33 \frac{p \Delta x}{q B L^2 \sin \alpha} \quad p \text{ in } GeV/c; \; B \text{ in } T; \; \Delta x \text{ and } L \text{ in } m$$

and $\left(\frac{\Delta p}{p}\right)_{ms}$ is given by equation 2. The errors in the determination of the angle α, which contribute to the error in the measurement of the momentum by the sagitta method, have not been included. They are given by formulae 3 and 4 and should be added in quadrature to the expressions above.

2   Magnet geometries

For applications in particle beams three different geometries are generally considered for detector magnets: dipolar, solenoidal and toroidal. In

strict terms, solenoidal magnets create a dipolar field too, but the above classification is justified by the geometrical arrangement of the magnetic field with respect to the direction of the particle beam.

2.1 Dipolar magnets

They are used to produce a uniform magnetic field orthogonal to the average direction of the particles whose momentum must be measured, actually their bending power is maximized for the particles emitted orthogonally to the magnetic field direction. These magnets are employed both in fixed target and collider experiments.

In fixed target experiments the interaction point is located outside the magnetic field region; the yoke and the winding shape must generally allow for the free passage of the particles through the useful magnetized volume in order to minimize multiple scattering and the probability of any unwanted interaction in passive media (air-core dipoles).

Iron-core dipoles can be used for high-energy muon spectrometry because they combine the necessity of a hadron absorber with a lower power consumption, as compared to air-core dipoles, though their momentum resolution is worse than that achieved by means of air-core magnets because of multiple scattering. The H-type and C-type configurations for air-core dipole magnets are schematically represented in figs. 1a and 1b, respectively, while an iron-core dipole is shown in fig. 1c.

In collider experiments the interaction point is located inside the magnetic field region and detector coverage as close as possible to 4π is required. The iron return yoke can be used as a hadron calorimeter and in this case completely encloses the magnetic field region (see figs. 2a and 2b). The transverse bending power is maximum in the backward and forward regions; there we take:

$$\int B_\perp dl \simeq B\frac{L_{gap}}{2}\sqrt{1+\tan^2\theta\sin^2\phi} \tag{5}$$

where L_{gap} is the length of the air gap along the direction of the beam, θ and ϕ are the polar and azimuthal angles defining the directions of the produced particles (see fig. 2c).

Since the particles of the circulating beams are also bent, two compensating magnets are required downstream and upstream the detector. This configuration cannot be used in electron-positron colliders because it would induce unacceptably intense synchrotron radiation.

2.2 Solenoidal magnets

They produce a magnetic field parallel to their axis which is made to

4

coincide with the average direction of the particles. This configuration is mainly used for collider experiments, with its axis coincident with the direction of the colliding beams, because of its good symmetry. Its transverse bending power is maximum in the barrel region ($\theta_{max} < \theta < 180^o - \theta_{max}$ - see fig. 3), where

$$\int B_\perp dl \simeq BR_{sol}$$

while, in the forward regions ($0^o < \theta < \theta_{max}$ and $180^o - \theta_{max} < \theta < 180^o$ - see fig. 3), varies according to the law:

$$\int B_\perp dl \simeq BR_{sol}\frac{\tan\theta}{\tan\theta_{max}}$$

where $\theta_{max} = \arctan(2R_{sol}/L_{sol})$ and R_{sol} and L_{sol} are the useful radius and the useful length of the solenoid (see fig. 3).

A solenoidal magnet does not deflect the circulating beams, therefore it can be installed also in electron-positron colliders and bending magnets for orbit correction are not required. However a solenoid induces a rotation of the beams with respect to their axes and has a focusing action on them. This action can be compensated by means of skew quadrupoles or solenoids.

2.3 Toroidal magnets

They generate a magnetic field with flux lines closed around the axis of the torus which is oriented parallel to the average direction of the particles. They are employed for both fixed target and collider experiments. Their bending power varies as [DUI90][GOE90]:

$$\int Bdl \propto \frac{1}{\sin\theta} \quad \text{with } \theta_{min} < \theta < \theta_{max} \tag{6}$$

in the case of a pure toroidal field (see fig. 4a and section 3.3). In colliding beam experiments, where about a 4π solid angle coverage is provided by toroidal magnets (see fig. 4b), expression 6 approximately holds for $\theta_{min} < \theta < \pi/2$, almost independent of the actual geometry of the detector magnets.

Toroids are mainly used as muon spectrometers with iron-core (see fig. 5). The introduction of iron in the magnetized region allows an enormous reduction of the current needed to provide a determined magnetic induction and provides a hadron absorber, though at the cost of a poorer momentum resolution.

Recently a special air-core toroid with uniform bending power, envisaged for the measurement of the charge-sign and of the momentum of hadrons and leptons up to 10 GeV, has been built at CERN for the fixed target experiment CHORUS [CHO94] (see fig. 6 and section 3.3). The pulsed operation of the magnet permits the use of thin aluminium wind-

ings, therefore enhancing the transparency of the coils. An air-core super-conducting toroid has been presented as a possible option for the precise measurement of muon momentum in the proposed ATLAS experiment at LHC [ATL92].

The magnetic field generated by the torus vanishes along its axis and therefore no compensating magnets are required in case of installation of such torus in colliders.

3   Magnet design considerations

3.1 Dipole magnets

  - *Air-core dipole magnets for fixed target experiments*

In air-core dipoles a fringe field is always present around the pole edges, this sets constraints on the position and on the design of the detectors nearby. In this respect the physical aperture of the magnet must fit as close as possible the detection volume, the coils must be placed close to the pole faces (see figs. 1a and 1b) and their sizes optimized according to air gap geometry and size. This also reduces manufacturing and operating costs.

The integrated transverse component of the magnetic field for an air-core magnet of the type shown in figs. 1a and 1b is given by:

$$\int B_\perp dl = B_o(l_p + \Delta l)$$

where:

-   B_o is the magnetic induction in the centre of the dipole gap;
-   l_p is the length of the pole pieces;
-   $\Delta l = k_l g$, where g is the gap height and $k_l \simeq 0.6 \div 1.2$ depending on winding position and cross section.

The number of ampere turns NI required to generate the magnetic induction B_o in the centre of the dipole, in the case when the return yoke is not saturated (iron permeability $\simeq \infty$), is given by:

$$NI \simeq \frac{B_o g}{\mu_o} \quad \text{(SI units)} \tag{7}$$

where μ_o is the magnetic permeability of vacuum. To avoid saturation the overall cross section of the return yoke S_{yoke} must be such that the magnetic induction does not exceed about 1.8 T. For a dipole with coils near to the pole faces (see figs. 1a and 1b) we have:

$$S_{yoke} = \frac{B_o}{1.8}(S_{pole} + k_t \ g \ P) \quad B_o \text{ in } T \tag{8}$$

where S_{pole} is the surface of the pole, P is the pole perimeter and k_t is a coefficient which depends on the geometry of the coils and

takes into account the dispersed magnetic flux, $k_t \simeq 0.5 \div 0.6$ for optimized configurations. The actual number of ampere turns required to generate the magnetic induction B_o in the centre of the dipole will be higher than that quoted in expression 7 because of the finite permeability of the iron yoke. This difference will increase at higher fields but is normally kept below $10 \div 15\%$ of the value given by expression 7.

H-type magnets are slightly more efficient than C-type ones in the generation of a magnetic field in a fixed volume because of the more symmetric yoke and the shorter flux lines. They are also lighter, require less space and close to iron saturation generate a more uniform field, on the other hand C-type geometry allows an easier access to the magnetized volume. H-type dipoles should normally be preferred to C-type ones every time geometrical constraints do not forbid this choice.

- *Iron-core dipole magnets for fixed target experiments*
  They are generally operated at the iron saturation limit (about $1.8 \div 2\ T$). The number of ampere turns required to generate a magnetic induction B in the iron yoke is less well defined as compared to the case of air-core magnets (for whom the assumption of infinite permeability of the iron in the return yoke is a good approximation to reality in the case of a non-saturated yoke) because of the non-linear behaviour of iron and the rapid variation of the magnetic permeability in the saturation limit. A rough evaluation can be obtained from:

$$NI \simeq \frac{B L_c}{\mu_o \mu_r} \quad \text{(SI units)}$$

  where L_c is the length of the integration path along a reference field line (see fig. 1c) and μ_r is an average value of the magnetic permeability along that line; $\mu_r \simeq 100$ for low-carbon steel (which is generally used for detector magnets) at magnetic induction around $1.9\ T$.

- *Air-core dipoles for collider experiments*
  In these magnets the useful magnetic volume is limited by the iron pole faces and by the windings uniformly distributed between the poles (see figs. 2a and 2b). The field is practically uniform in such a volume.
  Equation 2 is still valid and equation 8 becomes

$$S_{yoke} = \frac{B_o}{1.8} \left(S_{pole} + P \frac{t}{2} \right) \quad B_o \text{ in } T \qquad (9)$$

7

for an optimized design, where t is the thickness of the coil. In this case S_{yoke} is the net overall cross section of the iron, i.e. that one excluding the cross section of the active medium (if any) used for hadronic calorimetry.

3.2 Solenoids

The magnetic induction in a solenoidal magnet with non-saturated soft iron end caps is approximately uniform and the number of ampere turns NI required to provide a magnetic field B in the aperture is given by:

$$NI \simeq \frac{B \cdot h}{\mu_o} \quad \text{(SI units)}$$

where h is the distance between the pole faces (end caps). Also in this case the end caps and the iron return yoke can be used as hadron calorimeters and equation 9 still holds.

3.3 Toroidal magnets

These magnets do not require any return yoke since the field lines are closed around the axis of the toroidal coil. The azimuthal uniformity of the magnetic induction requires a uniformely distributed coil, in this case the magnetic induction for a constant permeability μ_r over the magnetized medium is given by

$$B(r) = \mu_o \mu_r \frac{NI}{2\pi r} \quad r_{in} < r < r_{out} \quad \text{(SI units)}$$

where r_{in} and r_{out} are the inner and outer radii of the toroid, respectively.

The toroid can be partially filled with iron in order to enhance the magnetic induction. Full iron-core toroids, used up to the iron saturation limits, present low power consumption and a strong attenuation of the $1/r$ dependence as compared to air-core toroids.

The radial magnetic field dependence can be reduced by distributing radially the coil windings in order to provide an increasing number of ampere turns ($NI \propto r$) with increasing radius.

A uniform magnetic field with polygonal field lines closed around the symmetry axis can be obtained by disposing the windings of the coil in triangular patterns replicated around the axis and constituting a polygonal parallelepiped (see fig. 6 [CHO94]). In this case the magnetic induction is given by:

$$B = \mu_o \frac{NI}{P} \quad \text{(SI units)}$$

where P is the perimeter of the polygon and in each triangular sector the field is parallel to the outer polygon edge. For the configuration shown

in fig. 6 stray fields are negligible and all the magnet parameters can be determined from basic electromagnetism formulae.

The construction of large superconducting toroids poses severe mechanical problems connected with the stabilization of the coils against magnetic forces. This is particularly true for rectangular shape coils (e.g. the proposed air-core toroidal muon spectrometer for the ATLAS experiment [ATL92]).

4 Conductors

4.1 Normal conductors

The overall cross section of the winding must be chosen as a compromise between construction costs (requiring small cross sections) and low operation costs, the latter are determined by the power consumption (requiring large cross sections) and the duty factor of the magnet and by the expected lifetime of the experiment. For a given number of ampere turns the power consumption is approximately proportional to the current density; reasonable values for the average current density are: $5 \div 6 \ A/mm^2$ for copper and $3 \div 4 \ A/mm^2$ for aluminium, which are the normal conductors used for detector magnets. The resistivities of copper and aluminium versus temperature t are:

$\rho_{Cu} = 0.0175 + 3.9 \cdot 10^{-3}(t - 20)$
$\rho_{Al} = 0.028 + 4.0 \cdot 10^{-3}(t - 20)$
ρ in $\mu\Omega \cdot m$ and t in $°C$,

respectively.

Notwithstanding its higher resistivity, aluminium is less expensive and considerably lighter than copper (the densities of copper and aluminium are 8.96 g/cm^3 and 2.70 g/cm^3, respectively). Furthermore aluminium has longer radiation length ($X_{oAl} = 8.9 \ cm$) and longer nuclear interaction length ($\lambda_{I_{Al}} = 39.4 \ cm$) as compared to copper ($X_{oCu} = 1.43 \ cm$ and $\lambda_{I_{Cu}} = 15.1 \ cm$) [PDG94].

Power consumption is approximately independent from the number of turns n_t that the coil is subdivided in; for a given ampere turn number and a fixed winding volume, the resistance of the winding will be proportional to $n_t{}^2$. The ohmic resistance of the coil must be chosen so to avoid high voltages (too many turns) or high currents (too few turns). For detector magnets (which are generally operated DC or slowly pulsed) a convenient value of the resistance is $0.15 \div 0.5 \ \Omega$ for power consumptions ranging from a few kW to a few hundreds kW (the higher values correspond to lower power consumptions) and further less with increasing power consumption

(e.g. the ohmic resistance is 0.06 Ω for the UA1 magnet which dissipates 6 MW).

4.2 Superconducting cables

The most frequently used superconducting alloys are Nb-Ti and Nb-$_3$Sn; the curves of their critical current densities as a function of the magnetic induction, at $4.5^\circ K$ and for Nb-Ti also at $2^\circ K$, are given in fig. 7 [LEB89]. From this picture one can see that superconductors can stand current densities by two or three orders of magnitude higher than normal conductors operated in DC mode. Nevertheless superconducting cables (generally consisting of bundles of Nb-Ti filaments in a copper matrix) are embedded in copper or in aluminium to provide their thermal stabilization [KAT89][MES89] therefore the average current density eventually varies in the range $40 \div 50$ A/mm^2.

4.3 Choice between normal and superconducting magnets

The choice between superconducting and normal conducting magnets is generally not univocal and results from a compromise among cost, technical and physical considerations. The expected operating time of the magnet and the cost of the electric power must be taken into account in the cost comparison between these two solutions. Conventional magnets are less expensive than superconducting ones for relatively weak fields ($< 6 \div 7$ kG) and small detection volumes (up to a few m^3). Superconducting magnets are preferable when strong fields ($> 1.2 \div 1.5$ T), large volumes (of the order of several tens of m^3 or larger) and long foreseeable operation time are required. For large volumes and fields ($> 2T$) only superconducting magnets are conceivable.

Superconducting magnets also offer the advantage of having coils of smaller thickness in terms of radiation and absorption lengths, but require a greater design effort and a longer construction time as compared to conventional magnets.

5 Cooling
5.1 Normal conducting magnets

DC magnets are usually cooled by forced water flow in hollow conductors. The water must be demineralized (conductivity $\simeq 1$ mS/cm) to avoid stray currents and consequently corrosion, deposition and obstruction of the cooling circuit.

The cooling water flow G corresponding to a power N is:

$$G \simeq \frac{N}{4.2\Delta t} \quad G \text{ in } \ell/s, \ N \text{ in } kW \text{ and } \Delta t \text{ in } {}^{\circ}C$$

where Δt is the allowed temperature increase of the water. The corresponding velocity of the water in the cooling circuit is:

$$v_c \simeq \frac{10^3 G}{A_h} \quad v_c \text{ in } m/s, \ G \text{ in } \ell/s \text{ and } A_h \text{ in } mm^2$$

where A_h is the area of the conductor hole. The pressure drop in the cooling circuit is [BOV70]:

$$\Delta p \simeq 4.8 \cdot 10^{-5} \frac{L_c v_c^{1.75}}{d_h^{1.25}} \quad \Delta p \text{ in } atm; \ L_c \text{ in } m; \ v_c \text{ in } m/s \text{ and } d_h \text{ in } m$$

where L_c is the length of the water circuit,

$$d_h \simeq \frac{4A_h}{P_h}$$

and P_h is the perimeter of the cooling hole; d_h coincides with the diameter of the hole in the case of a circular cross-section of the cooling circuit.

The size of the cross section of the cooling circuit and the number n of parallel cooling circuits must be determined taking into account that the maximum velocity of the water and the maximum pressure drop should not generally exceed $2 \div 6 \ m/s$ and $10 \div 15 \ atm$, respectively, and that

$$G \propto n^{-1}$$
$$v \propto n^{-1}$$
$$\Delta p \propto n^{-2.75}.$$

5.2 Superconducting magnets

The conductor of superconducting detector magnets is cooled by means of liquid helium at $4.3 \div 4.5 \ {}^{\circ}K$ (liquid helium under saturated vapour pressure) circulating either inside the conductor by forced flow or in pipes soldered onto the support aluminium cylinder (*indirect cooling*) by forced flow or thermosiphon method. Thermal insulation is provided by enclosing the coil in vacuum and inserting between the conductor and the vacuum chamber a screen cooled down to approximately $70{}^{\circ}K$ by liquid nitrogen and to even lower temperatures by helium vapour. Several tens of sheets of aluminized mylar are interposed between the conductor and the screen and between the latter and the vacuum chamber walls, in order to minimize radiative heat transfer (*superinsulation*). Superinsulation typically reduces the heat flux between the vacuum chamber walls and the screen to $1 \div 2 \ W/m^2$ [LEB89] and that between the screen and the conductor to approximately $0.5 \ W/m^2$ (see for example ref. [BAZ88]).

A liquid helium cryoplant for superconducting magnets is generally

operated in both *refrigerator* and *liquefier* modes between the temperatures $T_a = 4.3 \div 4.5°K$ and $T_b = 300°K$:

- in the *refrigerator* mode the cryoplant supplies its load with a flow of liquid helium (at the temperature T_a) which is vaporized in the load and returned to the plant at the same temperature T_a.
- in the *liquefier* mode the vaporized helium is fed back to the plant at the higher temperature T_b. This is the case of the cold helium gas evaporated from the current leads, which is used for counter-flow cooling along the leads themselves up to the room temperature end. In this way the specific heat inleak associated with the current leads can be reduced to about 1 W/kA.

Operation in the *liquefier* mode offers the advantage of intercepting heat at higher temperatures (the amount of absorbed heat per mass unit of boiling liquid helium, when warmed to room temperature, is 76 times that intercepted during vaporization at $4.3 \div 4.5$ °K), nevertheless it is more expensive than operation in the *refrigerator* mode. To compensate the rate of liquid helium vaporized by 1 W heat inleak in the $4.3 \div 4.5$ °K range, 1.5 $\ell/hour$ of liquid helium (*liquefaction duty*) must be produced by the cryoplant. This is equivalent (*entropy equivalent*) to about 6 W isothermal refrigeration at $4.3 \div 4.5$ °K (*refrigeration duty*). A *liquefier* is therefore approximately 6 times more power consuming than a *refrigerator* assuming that the two machines, working between the same temperatures, are characterized by the same thermodynamical efficiency [LEB89].

The investment cost C (in $MCHF$) of a plant producing helium cooling power P (all loads converted to entropy equivalent at 4.5 °K, in kW) can be estimated by a simple formula [SCH88] developed from price quotations received in recent years for helium cryoplants in the range of a few hundreds of watts to a few kilowatts. It contains a constant element for infrastructure and control equipment, a linear term for the gas compression and a square-root term for the cold production box:

$$C = 0.5 + 0.5P + P^{0.5}$$

In addition, also the running cost of the cryoplant must be taken into account; typically half of it is manpower and maintenance cost and the other half the cost of electricity. Ideally a cryoplant could achieve the *Carnot efficiency*

$$T_{cold}/(T_{warm} - T_{cold}) = 4.5/295 = 1/65$$

for producing 4.5 °K cooling, but in reality cryoplants come only to $10 \div 25\%$ of this figure [LEB89]; for plants in the 100 W cooling power range

$400 \div 600$ W of electricity have to be counted for cooling 1 W at 4.5 $°K$; for plants in the kilowatt range the corresponding figure is $250 \div 350$ W.

6   Magnetic shielding

Shielding is often required to protect electronic equipment installed near big detector magnets from magnetic fields. Shielding is usually provided by using very high-permeability materials, e.g. nickel-iron based alloys with $\mu_r = 10^4 \div 10^6$ such as mu-metal. All these materials must be treated at very high temperatures (1100 $°C$) after shaping. Some amorphous metals, which have the same magnetic properties of the nickel-iron alloys and are easier to use and less sensitive to plastic deformations, are available only in the form of very thin sheets (< 25 μm) of limited width (< 100 mm). These high-permeability materials have low saturation induction and therefore must be used in the presence of weak stray fields (smaller than a few mT). In the presence of stronger magnetic fields a supplementary shield, surrounding that made of the high-permeability material, must be used.

A selection of ferromagnetic materials which can be used for shielding is given in Table 1 as a function of the magnitude of the parasitic induction. η_{max} is the ultimate shielding efficiency which can be obtained with the corresponding material and it is defined as the ratio of the magnetic induction outside the shield (B_{out}) to that in the region surrounded by the screen (B_{in}).

These materials are formed in the shape of a completely or almost completely closed box surrounding the equipment or of plates or cylinders placed near the equipment. While in the first case the magnetic field inside the box vanishes completely or reduces to negligible values, in the second case an effective shielding is limited to a small region near the shield and is proportional to its size.

Table 1. Selection of magnetic materials for shielding [BIL92]

B [T]	Material	μ_{rmax}	η_{max}
> 1.5	low-carbon steel	< 3000	750
> 1.0	silicon steel	5000	1300
< 1.0	50 % Ni-Fe	7.5×10^4	2×10^4
< 0.5	80 % Ni-Fe	4×10^5	10^5
	Metallic glass	$> 10^5$	
	$(Fe_{40}Ni_{40}P_{14}B_6)$		

In the case of an infinitely long hollow cylinder placed in a uniform magnetic field transverse to the axis of the cylinder, in the non-realistic approximation of a uniform magnetic permeability $\mu_r \gg 1$, the shielding efficiency is given by [BIL92]:

$$\eta_\infty \simeq \frac{B_{out}}{B_{in}} = \frac{\mu_r}{4}\left(1 - \frac{a^2}{b^2}\right)$$

where a and b are the inner and outer radii of the cylinder, respectively. In particular

$$\eta \simeq \frac{\mu_r t_s}{2b} \quad \text{if } 2b \gg t_s$$

where $t_s = b - a$ is the thickness of the shielding.

The shielding efficiency of a cylinder of finite length $L > 8b$ is larger than 90 % of η_∞ over a length of $4b$.

The shielding efficiency can be enhanced by subdividing the magnetic material in layers separated by air gaps.

A typical example of shielding is that of photomultipliers; this is usually achieved by means of two coaxial cylinders, of which the external one (usually made of low-carbon steel) is thicker and reduces the magnetic field by a large factor and the inner one, with very high permeability but lower saturation induction (mu-metal or similar alloy, see Table 1), further abates the magnetic field to negligible values.

Cables carrying currents in one direction only cannot be shielded; therefore the input and output cables of magnets should be placed possibly together in order to avoid the generation of field lines around them.

7 Acknowledgments

reading of the manuscript. The contributions of A. Lutke and G. Pierantoni (CERN) to the preparation of the figures are also kindly acknowledged.

References

[ATL92] The ATLAS Collaboration, *Letter of Intent for a General-Purpose pp Experiment at the Large Hadron Collider at CERN*, CERN/LHCC/92-4 LHCC/I2 (1992)

[BAZ88] J.M. Baze et al., IEEE Trans. Magn., 24 (1988) 1260

[BIL92] J. Billan, *Materials*, Proceedings of the CERN Accelerator School on Magnetic Measurement and Alignment, Montreux, Switzerland, 16-20 March 1992, S. Turner ed., CERN 92-05 (1992) 17

[BOV70] C. Bovet, R. Gouiran, I. Gumowski and K.H. Reich, *A selection of formulae and data useful for the design of A.G. synchrotrons*, CERN/MPS-SI/Int. DL/70/4 (1970)

[CHO94] F. Bergsma et al., *The hexagonal air-core magnet of the CHORUS detector*, to be published in Nucl. Instr. and Meth.

[DUI90] P. Duinker and K. Eggert, *Muon detection at the LHC*, Proceedings of the ECFA Large Hadron Collider Workshop, Aachen, Germany, 4-9 October 1990, G. Jarlskog and D. Rein, eds., CERN 90-10 (1990) Vol. I, 452

[FAB94] C.W. Fabjan, *Detectors for elementary particle physics*, CERN-PPE/94-61 (1994)

[GLU63] R.L. Gluckstern, Nucl. Instr. and Meth., 24 (1963) 381

[GOE90] U. Goerlach, *Toroidal Field Geometries for LHC Muon Spectrometers*, Proceedings of the ECFA Large Hadron Collider Workshop, Aachen, Germany, 4-9 October 1990, G. Jarlskog and D. Rein, eds., CERN 90-10 (1990) Vol. III, 504

[KAT89] H.H.J. ten Kate, *Practical superconductors*, Proceedings of the CERN Accelerator School on Superconductivity in Particle Accelerators, Haus Rissen, Hamburg, Germany, 30 May - 3 June 1988, S. Turner, ed., CERN 89-04 (1989), 252

[KLE86] K. Kleinknecht, *Detectors for particle radiation*, Cambridge University Press, Cambridge (1986)

[LEB89] Ph. Lebrun, *Cryogenic systems*, Proceedings of the CERN Accelerator School on Superconductivity in Particle Accelerators, Haus Rissen, Hamburg, Germany, 30 May - 3 June 1988, S. Turner, ed., CERN 89-04 (1989), 41

[MES89] K.-H. Meß and P. Schmüser, *Superconducting accelerator magnets*, Proceedings of the CERN Accelerator School on Superconductivity in Particle Accelerators, Haus Rissen, Hamburg, Germany, 30 May - 3 June 1988, S. Turner, ed., CERN 89-04 (1989), 87

[PDG94] Particle Data Group, *Review of particle properties*, Phys. Rev. 50D (1994) 1173

[SCH88] J. Schmid, CERN, 1988; private communication

[YUA61] L.C.L. Yuan and C. Wu, *Nuclear Physics*, in Methods of Experimental Physics, L. Marton ed., Academic Press, New York (1961), Vol. 5, Part A

(a)

B_o

(b)

B_o

(c)

B
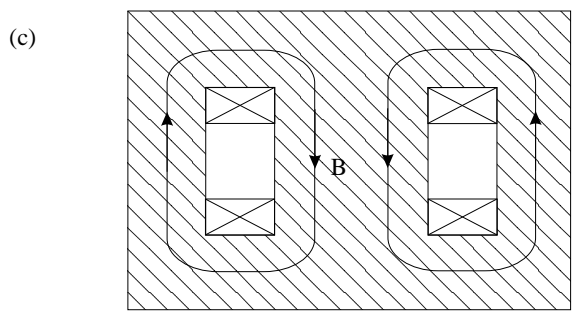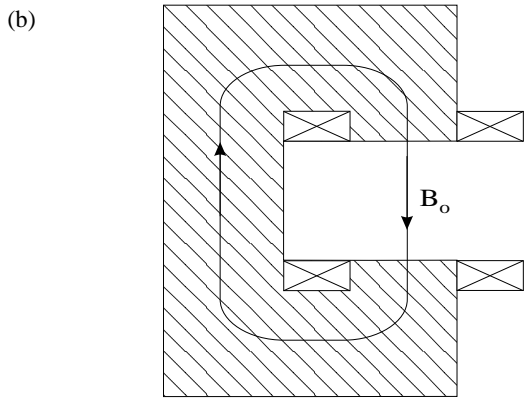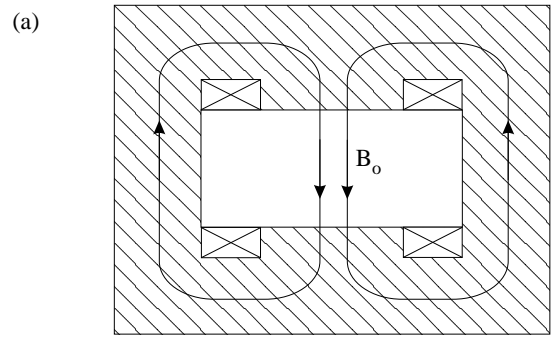
⊠ COIL   ⊠ IRON

Figure 1: Schematic designs of dipoles for fixed target experiments. (a) H-type air-core dipole; (b) C-type air-core dipole; (c) iron-core dipole.
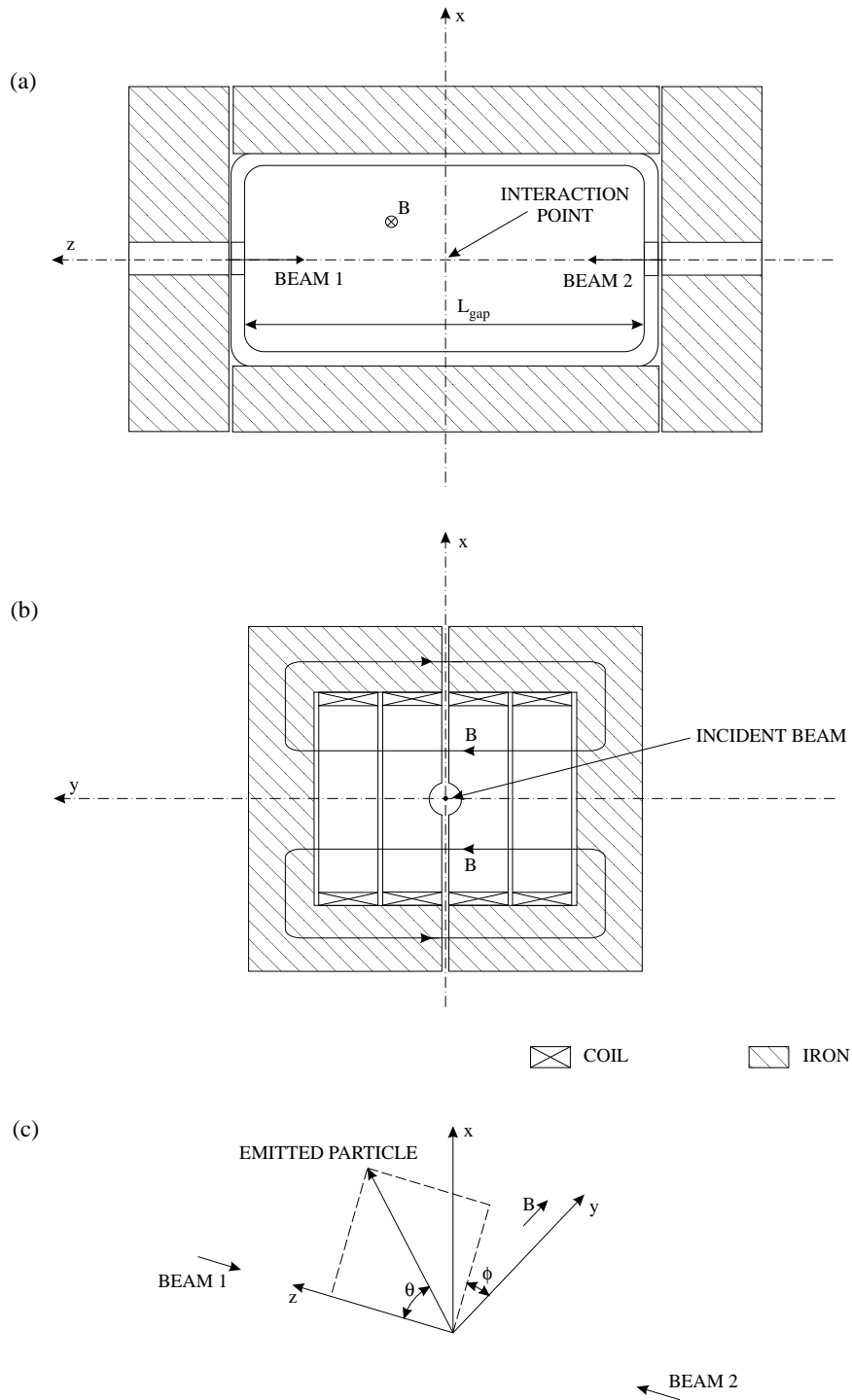
Figure 2: Dipolar magnet for collider experiments. (a) and (b) schematic cross sections; (c) definition of the angles θ and ϕ which determine the trajectory of a particle generated at the interaction point and the corresponding bending power (see expression 5).
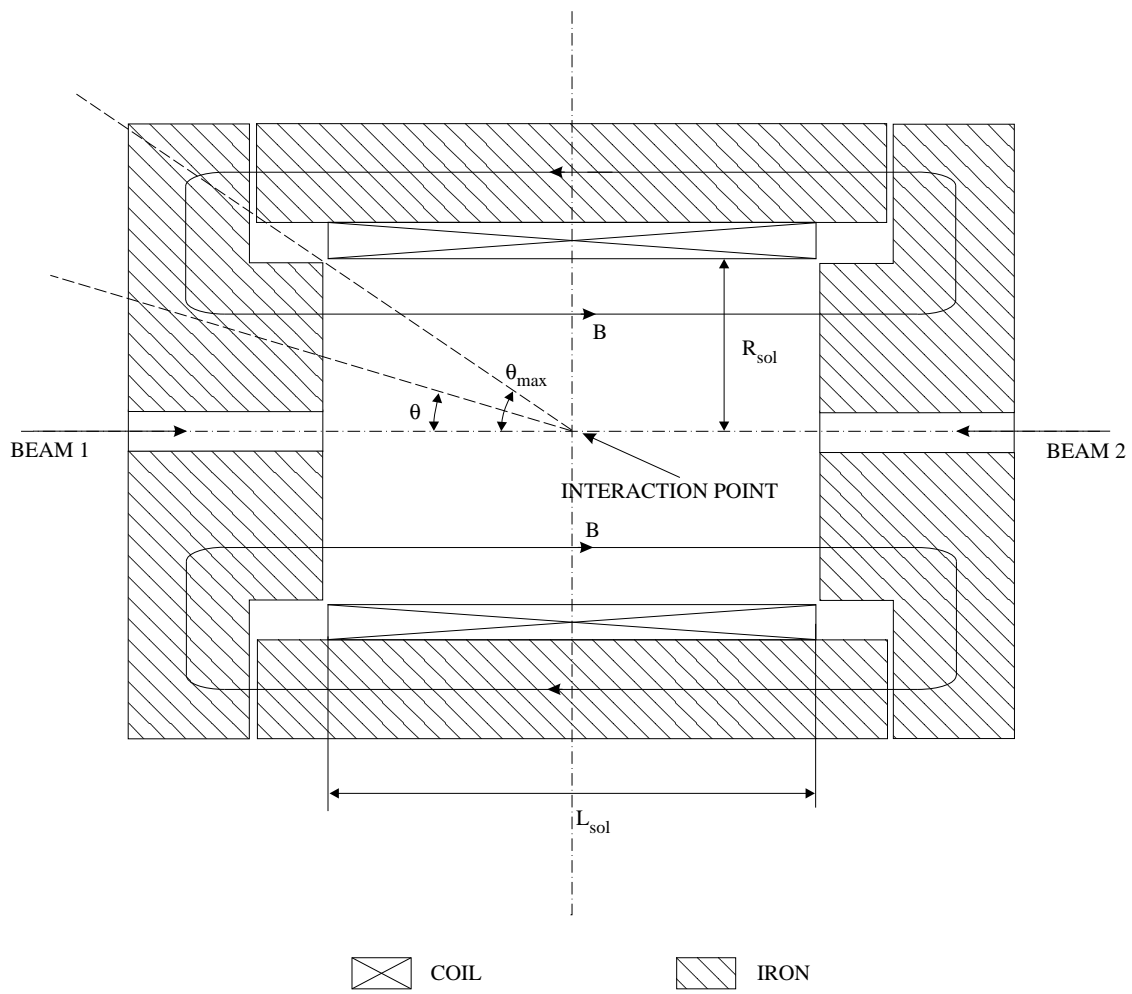
Figure 3: Schematic cross-section along the axis of a solenoidal spectrometer.
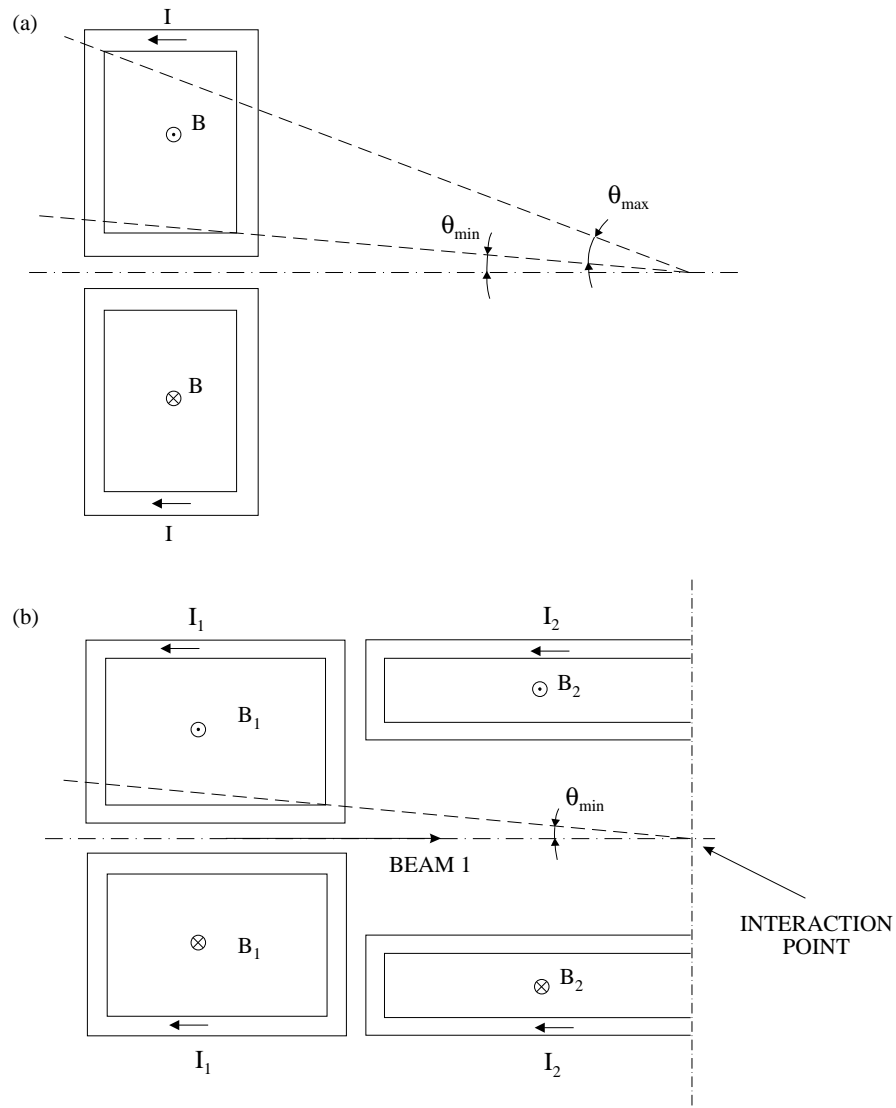
Figure 4: Schematic view of a toroidal field geometry for (a) fixed target, (b) collider (half detector) experiments.
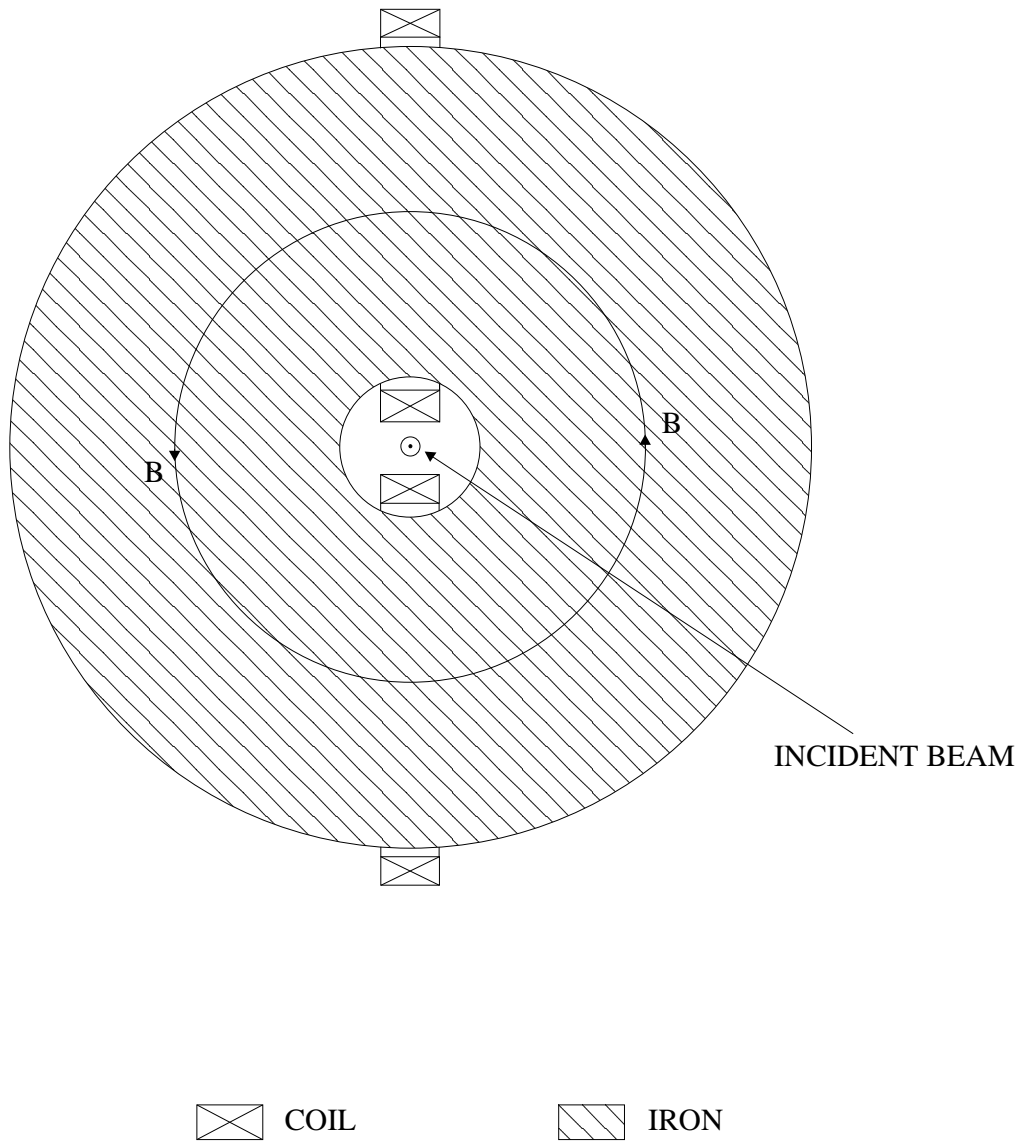
B

B

INCIDENT BEAM

⊠ COIL   ▨ IRON

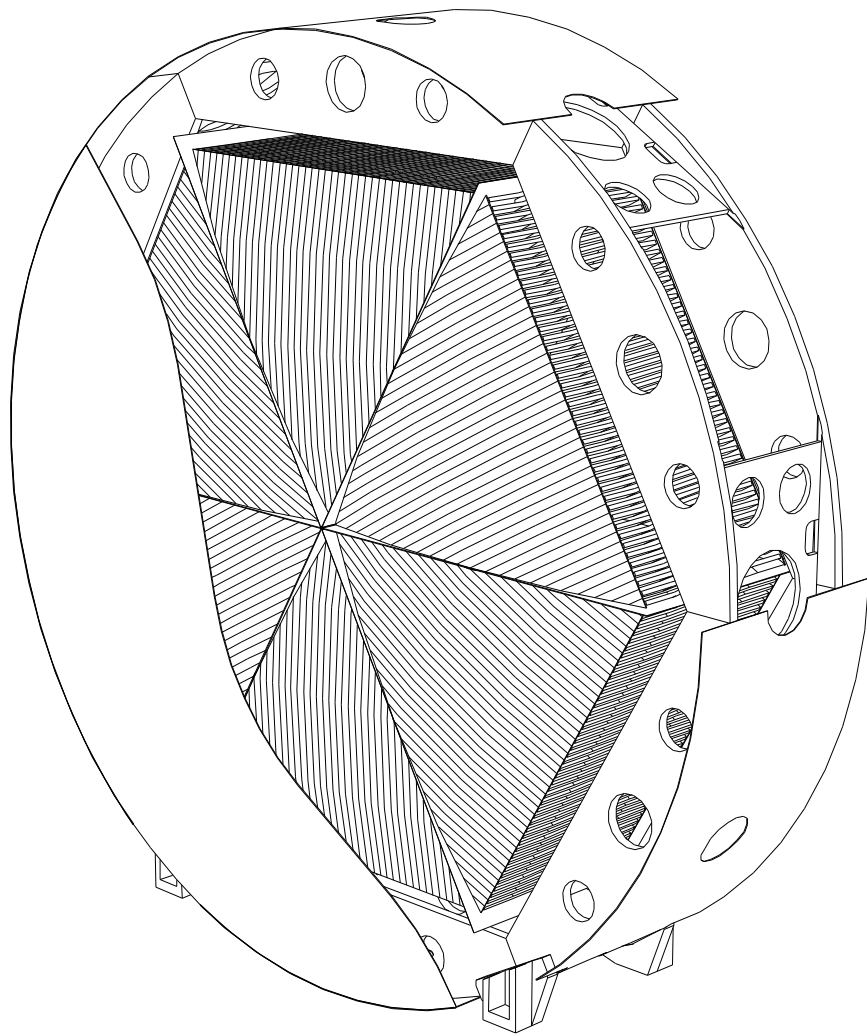Figure 5: Schematic cross section of an iron-core toroid for fixed target experiments.

Figure 6: The toroidal magnet for the CHORUS experiment at CERN [CHO94].
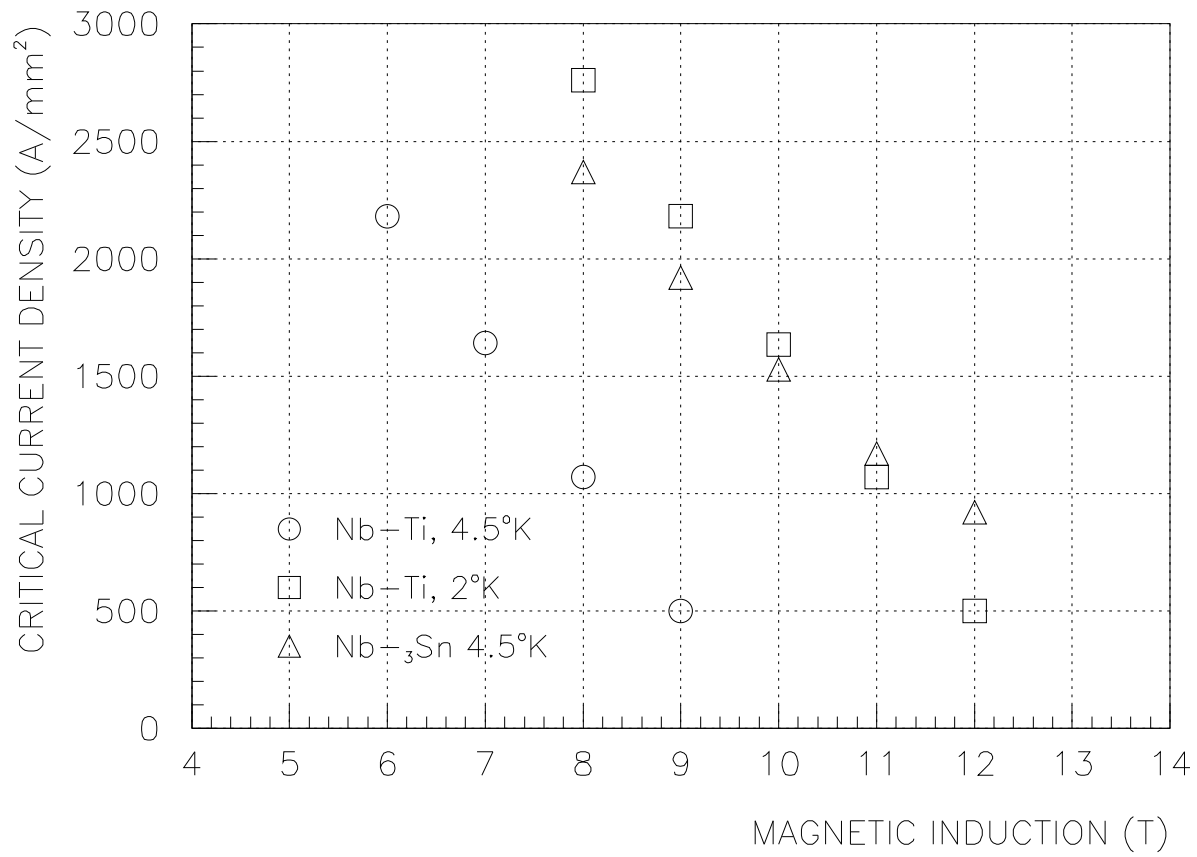
Figure 7: Critical current densities of Nb-Ti and Nb-₃Sn superconductors vs. magnetic induction (adapted from ref. [LEB89]).